# End bearing response of open-ended pipe piles embedded in rock

Mustafa Jafari[1], Haythem Gharsallaoui, Karl Henry Victor, Alain Holeyman

Université catholique de Louvain, Louvain-La-Neuve, Belgium

## Abstract

Prediction of bearing capacity of steel pipe piles in rock masses is an important consideration in civil engineering especially as such prediction influences the safety of the supported superstructures as well as the pile integrity in pile driving operations. Provided that the rock mass is described as a linear elastic and perfectly plastic material obeying the Hoek-Brown failure criterion, a finite element analysis is performed to investigate the embedment depth effect on the annular base bearing capacity and the failure mechanism of typical open-ended pipe piles in sedimentary rock masses. The pipe pile has smooth walls and rough toe surface. Annular toe resistance of pipe piles can serve as an estimate of the rock mass resistance to driving in a fully coring mode which is usually expected for large diameter open-ended pipe piles. Pipe pile results are also extended to circular piles and embedded strip foundations socketed in rock masses. The analysis is shown to highlight the influence of the annular geometry of the pipe pile causing an unsymmetrical failure mechanism with respect to pipe wall center as well as an inclination of rock mass reaction, which if sufficiently large, may lead to pile convergence and damage during pile driving operations. The failure mechanism legitimates the plug tendency to rise up in the pipe and explains the plug formation. The study demonstrates that in most practical applications, the bearing capacity of pipe piles approaches a limiting value, which is less than or at most equal to the end bearing capacity of an embedded strip foundation of width equal to the pipe wall thickness. A comparison has been made with experimental data. It is shown that the FE

[1] Corresponding author at: UCLouvain/iMMC/GCE, Place du Levant 1, 1348 Louvain-la-Neuve, Belgium
E-mail address: mustafa.jafari@uclouvain.be

results are relatively in good agreement with test data in terms of rock mass resistance and the mechanism of rock plug formation.

*Keywords*: Driven pipe in rock; bearing capacity of pipe pile; pipe pile plug; pipe pile refusal, rock-socketed pile

## 1 Introduction

Pipe piles are an important category of foundations employed offshore for supporting vital infrastructures such as wind turbines, long-span bridges, and harbor terminals. They have attracted increasing attention due to their ease of installation. Assessing the bearing capacity of pipe piles in indurated formations is necessary to design critical infrastructures such as wind turbines mostly founded on pipe piles. Despite their use, not much is known about their base bearing response in indurated formations at different embedment depths.

In the design of the majority of foundation types in rock, the design engineer is primarily concerned by the structural strength of the foundation, which usually dominates the foundation capacity rather than the embedding medium. As a result, the bearing response of rock masses has received little attention. However, thin annular sections of steel pipes can resist high axial stresses, and thus one cannot assume that the embedding rock mass is able to offer the required toe resistance in order to ensure superstructure loads are transferred safely to the ground. Furthermore, to provide lateral stability, pipe piles have to penetrate rock formations more often, in particular, in offshore environments. To reach the necessary penetration depth, pile driving is an economical option. The installation of pipe piles requires estimating pile toe resistance to evaluate driving stresses and to avoid pile damage and refusal. This in turn helps to choose the right set of equipment and pipe dimensions. Thus an accurate prediction of the ultimate bearing capacity of the pipe piles is important for efficient pipe pile installation and design.

It is generally agreed that the ultimate bearing capacity of foundations increase with depth due to the surplus shearing resistance offered by the rock mass above the foundation bed level. It is common practice to socket piled foundations 2-3 shaft diameters into the rock mass to enhance the bearing capacity [1]. A common criterion to describe behavior of rock masses is the Hoek-Brown (H-B) failure criterion. Not much literature is available about the bearing capacity of foundations on rock masses obeying the H-B failure criterion considering embedment depth. Perhaps, one of the reasons is the later adoption of the H-B failure criterion for rock masses, which was first published in 1983 [2] with its latest version in 2002 [3]. Early attempts to predict the bearing capacity of foundations on rock masses have focused mostly on surface strip foundations applying traditional upper bound and lower bound theorems of limit analysis.

Kulhawy and Carter et al. [4] proposed a relationship for the lower bound to the ultimate bearing capacity of surface strip foundations on rock masses based on theorems of limit analysis. This lower bound was found by assuming the simplest stress field that satisfied both the failure criterion and the equilibrium equations. Later studies reveal that their solution significantly underestimates the bearing capacity. Merifield et al. [5] performed numerical upper bound and lower bound theorems of limit analysis for surface strip foundations by incorporating finite elements. They adopted a continuous approximation of the H-B failure criterion to account for the apex discontinuity in the failure envelope. They claimed that the true bearing capacity values are bracketed to within 2.5% between the lower and the upper bounds. Saada et al. [6] offered a slightly different approach according to upper bound theorems of limit analysis and non-linear optimization for a strip footing on rock masses obeying H-B failure criterion. The solutions were derived from direct analysis of the kinematically admissible failure mechanisms. They reformulated the H-B failure criterion as a nonlinear Mohr-Coulomb criterion with pressure-dependent cohesion and friction angle. Their results agreed closely with the results from [5]. Clausen [7] used standard displacement finite element method to determine the ultimate bearing capacity of surface circular foundations. He employed an exact version of the Hoek–Brown criterion without any approximations for the discontinuities in the failure surface.

Nevertheless, none of the above authors examined the embedment depth effects. To the author's knowledge, Serrano et al. [8,9] were first to present analytical solutions for the ultimate bearing capacity of piles with rough base and smooth shaft in rock masses obeying H-B failure criterion. Initially, they published their solutions for the 1998 version and later adopted the 2002 version. They made the following assumptions: (1) Postulated failure mechanisms are according to Meyerhof [10]. For a pile in weightless rock with practically no surcharge pressure, $q_0$, the failure mechanism extends to the ground level for shallow embedment and rests local for deep embedment as illustrated in Fig. 1. Such failure patterns have been long observed in experiments. (2) Theory of characteristic lines can be employed together with associated plasticity. The choice of the associated flow rule has long been used in soil and rock mechanics to make analytical approaches such as theorems of limit analysis work. (3) Bearing capacity of pile is obtained from a plane strain problem (embedded strip foundation) employing De Beer shape factors [11]. Two cases for the average surcharge pressure, $q_0$ on the assumed failure surfaces were considered: a) less than or b) greater than the uniaxial compressive strength of the intact rock mass $\sigma_{ci}$.

Firstly, this paper addresses the annular bearing response of open-ended pipe piles in an isotropic homogeneous material utilizing finite element (FE) method. The rock mass is weightless and obeys non-linear Hoek-Brown failure criterion. The primary focus will be the embedment effects on the ultimate toe bearing capacity and associated failure modes. The pile-soil interface is fully rough at the base and smooth along the shaft meaning that the pipe pile penetrates the rock mass in a fully coring mode. It has been shown that the tendency of driven open-ended steel pipe pile to penetrate in an unplugged mode increases as the diameter increases [12]. In addition, the pipe pile response is compared with piles and embedded strip foundations, which are indeed two extreme case of pipe piles. The former has an internal radius of zero while the latter has an infinite external radius.

Secondly, the numerical results are compared against test data from static penetration tests and impact-driven instrumented model pipe piles into natural/synthetic rock masses. Taken together, the results indicate a relatively accurate prediction of the pipe pile end bearing response as demonstrated by agreement with test data from model pipe piles. Furthermore, the results provide some insight on the mechanism of plug formation.

## 2 Problem description

The problem consists of investigating the annular bearing response of typical embedded pipe piles by employing an axisymmetric model. The boundary conditions for the axisymmetric pipe pile is depicted in Fig. 2(a) and the geometry details are provided in Table 1. A rigid pipe pile of thickness, $t$ (0.05 m) and variable external diameter $D_o$ is embedded at depth, $d$ in a homogeneous weightless isotropic rock mass whose strength and elastic properties are described in Section 3 – Constitutive model. Pipe piles are characterized by the ratio of the external diameter to the pipe thickness ($D_o/t$), which is often referred to as pipe dimension ratio. After reviewing catalogues from multiple pile manufacturers, it is found that most of the available pipe dimensions in the piling industry fall in the range of 18<$D_o/t$<130. With the lower and upper ranges for onshore and offshore applications, respectively. Here, two types of pipe piles are selected: $D_o/t$= 22 and 38. The former has $D_o$=27.31 and $t$=1.27 cm while the latter has $D_o = 182.9\ cm$ and $t = 5.1\ cm$ and is projected to be used as foundation for a jacket structure to support an offshore wind turbine of 10 MW rated capacity [13].

Results from these pipe piles are then compared with circular and strip foundations. The pipe pile will be referred to as a circular pile of radius, $t$ when $D_o/t$=2 and as a nearly-strip foundation of width, $t$ when

$D_o/t$=8000. The pipe pile approaches a strip foundation as $D_o \to \infty$. The foundation is pre-embedded to depth, $d$ which is varied at 0, 1, 2, 3, 4, 5, 6, 7, 8 times the pipe wall thickness, $t$. Idealizing the pipe as a rigid indenter, a prescribed downward displacement with a horizontal fixity is applied at the pipe toe bed level and the resulting average reaction is found. Let $q$ be the average pressure that the pipe annulus exerts on the rock mass, the ultimate value of $q$ (referred to as the ultimate annular bearing capacity) will be denoted as $q_u$.

Theoretically, the ultimate loads are defined when the slope of load-displacement curve drops to zero percent of the initial slope and a load-plateau is reached. Because of the numerical tool (Section 4.1) used in this paper, it is very time consuming to reach low values of relative slope. It is assumed that the ultimate annular bearing capacity is signaled when a settlement equal to 25% of the foundation wall thickness has occurred. As shown later, at this point the slope of the load-displacement curves fall below 1% of the initial value for the analyses conducted in this paper unless stated otherwise. As a result, the computed ultimate loads are sufficiently accurate for practical purposes.

In order to relate the ultimate toe bearing capacity of the pipe pile to intrinsic properties of the rock mass, it is practical to resort to a bearing capacity equation such as:

$$q_u = N_{\sigma 0}\, \sigma_{ci} \tag{1}$$

where $N_{\sigma 0}$ is a global bearing capacity factor, which accommodates the effects of rock intrinsic strength as well as embedment and pipe shape while $\sigma_{ci}$ is the uniaxial compressive strength of the intact rock. The global bearing capacity factor does not include the rock mass self-weight effects. For high quality strong rock masses, the rock weight would have a negligible effect on the ultimate toe bearing capacity of pipe piles due to their thin wall thickness [5].

## 3 Constitutive model

## 3.1 Hoek-Brown failure criterion

The rock mass has been modeled as a linearly elastic and perfectly plastic material obeying the Hoek-Brown (H-B) failure criterion [3], which is an empirical yield envelope obtained from extensive triaxial tests on a wide range of rock types. Adopting the sign convention that compressive stresses are positive, one can write

$$\frac{\sigma_1}{\sigma_{ci}} = \frac{\sigma_3}{\sigma_{ci}} + \left(m_b \frac{\sigma_3}{\sigma_{ci}} + s\right)^a \tag{2}$$

where $\sigma_1$ and $\sigma_3$ denote the major and minor principal stresses respectively; $\sigma_{ci}$ is the uniaxial compressive strength of the intact rock; $a$, $m_b$ and $s$ are the derived parameters defined according Eqs. (3), (4), and (5).

$$m_b = m_i \exp\left(\frac{GSI - 100}{28 - 14D}\right) \tag{3}$$

$$s = \exp\left(\frac{GSI - 100}{9 - 3D}\right) \tag{4}$$

$$a = \frac{1}{2} + \frac{1}{6}\left(\exp\left(-\frac{GSI}{15}\right) - \exp\left(-\frac{20}{3}\right)\right) \tag{5}$$

in which $GSI$ = geological strength index; $m_i$ = material constant; and $D$ = disturbance factor. $GSI$ is a rock quality parameter and depends on the joint and surface characteristics of the rock mass. It can be evaluated by visual appearance of the rock mass sample in laboratory or rock mass outcrop in the field.

The material constant, $m_i$ can be obtained from triaxial test data using statistical analyses. In the absence of laboratory data, it can be estimated for different rock types according to empirical charts and tables [14]. The disturbance factor accounts for stress relaxation and blast damage in the rock mass. The uniaxial compressive strength ($\sigma_c$) of the rock mass can be found by setting $\sigma_3$=0 in Eq. (2).

$$\sigma_c = s^a \sigma_{ci} \tag{6}$$

The uniaxial tensile strength ($\sigma_t$) can be found by setting $\sigma_1$ = 0 in Eq. (2) and solving the following equation for $\sigma_t$:

$$\frac{\sigma_t}{\sigma_{ci}} + \left(m_b \frac{\sigma_t}{\sigma_{ci}} + s\right)^a = 0 \tag{7}$$

Combining Eqs. (6) and (7), one can derive an equation for $m_i$

$$m_i = \left(s\frac{\sigma_c}{\sigma_t} - \left(\frac{\sigma_t}{\sigma_c}\right)^{\frac{1-a}{a}}\right) \exp\left(-\frac{GSI - 100}{28 - 14D}\right) \tag{8}$$

For intact rock ($GSI$=100), $m_i$ can be found from intact uniaxial tensile strength, $\sigma_{ti}$ and $\sigma_{ci}$ :

$$m_i = \frac{\sigma_{ci}}{\sigma_{ti}} - \frac{\sigma_{ti}}{\sigma_{ci}} \tag{9}$$

Eq. (9) has important practical applications since it correlates the $m_i$ parameter to intact uniaxial compressive and intact tensile strengths of a rock mass.

Another useful representation of H-B failure criterion is to express the instantaneous friction angle ($\phi_{inst}$) as a function of the confining stress ($\sigma_3$). This enables one to compare the frictional behavior of the material to that of a Mohr-Coulomb material with constant friction angle. $\phi_{inst}$ can be determined from the slope of the tangent ($p$) to the failure envelope in the principal stress plane by

$$\phi_{inst}(\sigma_3) = 2\left(\tan^{-1}\sqrt{p(\sigma_3)} - \frac{\pi}{4}\right) \tag{10}$$

where $\phi_{inst}(\sigma_3)$ is in radians. The slope of the tangent ($p$) is obtained by differentiating Eq. (2):

$$p(\sigma_3) = \frac{\partial\sigma_1}{\partial\sigma_3} = 1 + \frac{m_b a}{\left(m_b \frac{\sigma_3}{\sigma_{ci}} + s\right)^{1-a}} \tag{11}$$

Looking at (11), the $\phi_{inst}$ approaches zero as $\sigma_3$ approaches infinity. Theoretically, this means that that the H-B material changes from a frictional material to a cohesive material at very high confining stresses.

## 3.2 Flow rule

Performing elastoplastic calculation of bearing capacity problems requires a flow rule so that the increments of plastic strain increments can be calculated. The Hoek-Brown failure criterion is an empirical yield envelope.

Therefore, no original plastic potential function was defined. To specify the flow rule, some authors use associated plasticity, while some others use a constant dilatancy angle [14]. Some workers investigate the post-failure properties of rock masses by triaxial tests [15] . In such tests, the test specimens may undergo nonhomogeneous deformation modes leading to measurement of the mechanical response of a system rather than the real constitutive behavior of rock masses [16]. As a result, there is still much debate on post-failure properties of rock.

In this paper, we adopt the flow rule which is proposed by Carranza-Torres and Fairhurst [17]. This flow rule can capture some important aspects of rock dilatancy such as its dependency on confining stresses [18,19]. This flow rule uses a plastic potential function similar to that of Mohr-Coulomb failure criterion except that the dilatancy angle varies with $\sigma_3$. The plastic potential function writes as

$$G_{13} = S_1 - \frac{1 + \sin\psi_{mob}}{1 - \sin\psi_{mob}} S_3 \tag{12}$$

where $S_1$, and $S_3$ are scaled principal stresses, defined as

$$S_i = -\frac{\sigma_i}{m_b \sigma_{ci}} + \frac{s}{m_b^2} \quad for\ i = 1, 3 \tag{13}$$

and $\psi_{mob}$ is the mobilized dilatancy angle, varying with $\sigma_3$ from its input value , $\psi_{max}$ at $\sigma_3$=0 ( unconfined dilation angle) down to zero at a threshold confining pressure $\sigma_3 = \sigma_\psi$ as:

$$\psi_{mob} = \left(\frac{\psi_{max}}{\sigma_\psi}\right)(\sigma_\psi - \sigma_3), \qquad 0 \le \sigma_3 \le \sigma_\psi \tag{14}$$

To allow for plastic expansion in the tensile zone, an increased artificial mobilized dilatancy is used.

$$\psi_{mob} = \psi_{max} + \frac{\sigma_3}{\sigma_t}(\psi_{max} - 90^\circ), -\sigma_t \le \sigma_3 \le 0 \tag{15}$$

Fig. 3(a) visualizes the evolution of mobilized dilatancy angle ($\psi_{mob}$) as a function of $\sigma_3$. As can be seen in Eq. (14) and (15), the flow rule has two input parameters: (1) $\psi_{max}$ and (2) $\sigma_\psi$. The first parameter is the dilatancy angle at null confinement ($\psi_{max}$), which is assumed to be three fourth of the corresponding friction angle. Some authors have assumed $\psi_{max} = \phi_{inst}$ for null confinement [20]. Besides, $\psi_{max} = \frac{2}{3}\ \phi_{inst}$ is also proposed for high quality rocks [21].

The second flow rule parameter ($\sigma_{\psi}$) is determined by the x-intercept of a tangent line on the instantaneous friction angle curve in Fig. 3(a) starting from the $\psi_{mob}$=3/4 $\phi_{inst}$ at $\sigma_3 = 0$. A tangent line is chosen to avoid high levels of non-normality in the model, which could cause numerical instabilities. Since the difference between dilatancy angle and friction angle is mostly less than 20°, it can be expected that bearing capacity values are close to that calculated by associated plasticity [22].

The proposed linear mobilized dilatancy angle can be plotted using Eqs. (14) and (15). Similarly, $\phi_{inst}$ can be plotted according to Eq. (10). Knowing the value of $\psi_{max}$=3/4 $\phi_{inst}$ at $\sigma_3 = 0$, a set of equations can be established in order to solve for $\sigma_{\psi}$. Fig. 3(b) depicts the variation of the adapted flow rule parameters versus Hoek-Brown model parameters.

The validity of the adapted flow rule in this paper may arise some questions. However, it is believed that the current choice of flow rule has no effect on the conclusions of this paper, which focuses on unplugged base response of pipe piles. It has been shown that the dilatancy angle does not play an important role in response of insufficiently constrained problem like surface footings. The impact of dilatancy aggravates as problem becomes confined and kinematic restriction increases [23]. The failure mechanism of an unplugged pipe pile in this study is shown later (Fig. 7) to be similar a surface footing, hence it can be treated as an insufficiently constrained problem.

A related point to consider is that the adopted flow rule results is a non-associated flow rule. Theoretically the limit load may not be unique and may lie within an interval [24]. Hence, load-displacement curves can contain remarkable spurious perturbations and raggedness in the case of extremely non-associated problems [22,25–29]. As demonstrated later (Fig. 5), the calculated load-displacement curves of this study are in general fairly smooth without any spurious perturbation, it can be thus judged that the interval of feasible solutions is so narrow that has no practical significance.

### 3.3 Reference material

This paper examines the bearing capacity of pipe piles in a rock mass with $m_i$ = 1, 5, 7.5 and 10. This range corresponds to most sedimentary rock masses such as carbonates, clay stones, gypsum and chalk [14] as shown in Table 2. The rock masses are assumed intact and undisturbed, which is expected considering the size of typical piles to that of rock masses. As a result, one can set $GSI$=100 and $D$=0. Intact deposits of sedimentary rocks are often encountered offshore and onshore. Furthermore, it has been reported that disturbance factor, D has no practical effect on the bearing capacity of high when GSI =100 [6]. The dilatancy parameters are listed in Table 3. The Young's modulus of the rock mass, $E_{rm}$ can be found according to empirical relationships [30]. To cover the broad spectrum of sedimentary rocks, a ratio of $E_{rm}/\sigma_{ci}$=1000 and a Poisson's ratio $\nu$=0.2 are used. In the calculations, $\sigma_{ci}$ = 7 MPa is used. The choice of Poisson's ratio has been made according to the range of typical values for different rock types [31]. Since ultimate loads are investigated under fully developed failure mechanisms, the deformation characteristics of the rock mass do not affect the results.

## 4 Numerical procedures

### 4.1 Numerical tool

Plaxis 2D 2019 [32] is employed as the FE analysis tool for this axisymmetric boundary value problem. A small strain finite element analysis is conducted. The stress integration scheme employs the initial stiffness method, i.e. an elastic constitutive matrix is used instead of formulating any elastoplastic constitutive matrices. This can be computationally expensive due to higher number of iterations to converge. The initial stiffness method is preferred here since the elastoplastic constitutive matrices of failure criteria (e.g. H-B criterion) containing edge and apex discontinuities can pose certain numerical challenges unless special measures are taken [33–36]

All models were meshed with identical element size and type so that comparable results could be found. A zone of finer mesh equal to the pipe pile thickness, $t$ was also created around the embedded pile. Fig. 2(b) depicts the model domain and mesh for a pipe pile with $D_O/t$ = 38 embedded at $d/t$ = 8. Regarding the element types, six-node triangular elements with three Gauss points are used. Each node has two displacement degrees of freedom. Typically, the models contain 25000 nodes, and 12000 elements. The displacement increment is controlled by an automated load stepping procedure [37]. An elastic interface/joint element was placed beneath the pipe base in order to calculate the contact shear stresses. The elastic stiffness was set sufficiently high to avoid any kind of slip or gapping at the interface and ensure failure would occur in the rock mass. The normal and tangential stiffness was set to $K_N$=2139 GPa/m; $K_T$=194.4 GPa/m. This was high enough to keep any elastic displacements of the interface less than 0.5% of the prescribed displacement.

## 4.2 Convergence Analysis

To evaluate how results are affected by discretization errors, a convergence analysis is conducted using the method proposed by Cook [38] for finite element analyses. This method was also successfully used for calculation of bearing capacity of circular footings on a Hoek-Brown material [7]. In this process, the analysis is conducted with all parameters being identical except the finite element mesh which is refined in a consistent manner. The value of the ultimate load, $q_u$, for different normalized mesh densities are plotted as shown in Fig. 4. The normalized mesh density is defined as $h = 1/\sqrt{n_{DoF}}$ where $n_{DoF}$ is the number of degrees of freedom. A quadratic polynomial is fit to the data points with a high R-Squared value. With the polynomial it is possible to extrapolate to $h$=0 in order to obtain the convergence value for the ultimate bearing capacity as $n_{DoF}$ tends towards infinity ($h \rightarrow 0$). The value of the ultimate load seems to converge as the mesh is refined.

The convergence analysis was conducted for three geometries: $D_o/t$ = 22, 38, and 8000. For each geometry two embedment depths were considered, $d/t$=0 and $d/t$=7. The results are shown in Fig. 4 for the reference Hoek-Brown material with $m_i$=10. For the selected mesh in the FE analysis, the computed ultimate load lies within 4% of the convergence value. Since the pipe pile at surface ($d/t$=0) with $D_o/t$=8000 is approximately a surface strip footing and the pipe pile with $\mathrm{D_o/t}$=2 is circular surface footing, the bearing capacity values can be compared against some published bearing capacity values of surface circular and strip foundations, which are obtained using associated plasticity. Table 4 lists the bearing capacity values. As expected, the calculated bearing capacity values employing the adapted flow rule of this paper are close with the bearing capacity values using associated plasticity.

# 5 Results

## 5.1 Load-settlement curves

Typical normalized load-displacement diagrams of the pipe piles ($D_o/t$ = 22 and 38), circular pile ($D_o/t$=2) and nearly-strip foundation ($D_o/t$=8000) are illustrated in Fig. 5. Each diagram depicts the normalized load-displacement curves of the foundations pre-embedded at $d/t$ = 0, 1, 2, 3, 4, 5, 6, 7, and 8 in the reference Hoek-Brown material with $m_i$ =10. Recalling that a prescribed displacement equal to 25% of the pipe wall thickness is applied, one can note that theoretically the ultimate bearing capacity of the circular pile has not been mobilized beyond some embedment depth, $d/t$>2. The slope of the load-displacement curve does not fall below 5% of the initial slope. The results for the circular pile are provided for sake of completeness.

### 5.2 Failure patterns

Local failure mechanisms occur when a smoothly varying deformation pattern suddenly changes and that all further deformations are localized in the shear bands/slip planes/failure surfaces. This process is also referred to as strain localization. The small-strain finite element formulation is capable of capturing some important aspects of the failure mechanisms such as the orientation of the slip planes. However, the thickness of the slip lines are mesh dependent and are hence not useful [39]. Typical failure patterns of the pipe piles ($D_o/t$ = 22 and 38), circular pile ($D_o/t$=2) and nearly-strip foundation ($D_o/t$=8000) embedded in the reference H-B material with $m_i$=7.5 are illustrated in Fig. 6 by plotting for the last calculation step, the incremental deviatoric strain, $\varepsilon_q$ defined as:

$$\epsilon_q = \sqrt{\frac{2}{3}\left[\left(\epsilon_{xx} - \frac{\epsilon_v}{3}\right)^2 + \left(\epsilon_{yy} - \frac{\epsilon_v}{3}\right)^2 + \left(\epsilon_{zz} - \frac{\epsilon_v}{3}\right)^2 + \frac{1}{2}\gamma_{xy}^2\right]} \quad (16)$$

where $\varepsilon_{xx}$, $\varepsilon_{yy}$, $\varepsilon_{zz}$, $\gamma_{xy}$, are the Cartesian components of the strain increment and $\varepsilon_v$ = $\varepsilon_{xx}$+$\varepsilon_{yy}$+$\varepsilon_{zz}$ is the volumetric strain increment. For sake of clarity, only the failure patterns at normalized embedment depth, $d/t$ = 0, 2, 4, and 8 are shown.

In addition to being unsymmetrical with respect to pipe wall center, the failure mechanism of the pipe piles ($D_o/t$ = 22 and 38) extend to the ground level at shallow embedment ($d/t \le 4$). As embedment increases further, the failure mechanism becomes local and concentrated at the interior of the pipe pile. Intense bands of shearing deformation characterize the failure mechanisms for all the pipe pile dimensions. From the failure patterns, one can conclude that the true ultimate bearing capacity is mobilized when the failure mechanism extends to the surface. Fig. 7 demonstrates the effect of the Hoek-Brown parameter $m_i$ on the failure mechanisms. Decreasing $m_i$ results in failure patterns that are confined to the proximity of pipe wall.

### 5.3 Bearing capacity factor

Global bearing capacity factor, $N_{\sigma 0}$ versus normalized embedment depth, $d/t$ of the pipe piles ($D_o/t$ = 22 and 38), circular pile ($D_o/t$=2) and nearly-strip foundation ($D_o/t$=8000) are plotted in Fig. 8. For each value of the H-B parameter $m_i$, the analytical solution of $N_{\sigma 0} - d/t$ by Serrano et al. [9] for circular piles and strip foundations are plotted as well. A very low surcharge pressure, $q_0 = 1.4 \times 10^{-5}\, \sigma_{ci}$ is assumed since their analytical solution is not applicable for null surcharge (Fig. 1).

### 5.4 Depth factor

In order to better observe the variation of bearing capacity with respect to embedment depth for a given foundation with $D_o/t$, a depth factor can be defined by normalizing the bearing capacity factor ($N_{\sigma 0}$) at depth, $d$ against the surface bearing capacity factor ($N_{\sigma 0,S}$) as

$$d_{\sigma 0} = \frac{N_{\sigma 0}}{N_{\sigma 0,S}} \tag{17}$$

This depth factor has been plotted against embedment depth in Fig. 9.

## 6 Discussion

### 6.1 Bearing capacity enhancement and mechanism of plug formation

As it can be seen in Fig. 8 that the bearing capacity of the foundation types with dimension ratio, $D_o/t$ = 2, 22, 38, and 8000 increases with embedment depth. The bearing capacity factor increases at a relatively sharp rate up to a depth of $d/t$=1-2 as it can be seen in depth factor diagrams (Fig. 9). This justifies the existing practice in the industry to socket piles for a length of one to two pile diameters into the rock mass.

Moreover, the diagrams of the bearing capacity factor (Fig. 8) indicate that the bearing capacity of the pipe piles ($Do/t$ = 22, and 38) at shallow embedment ($d/t$<2-4) is slightly higher than that of strip foundation. This is because of the confinement introduced by the tubular pipe geometry, which makes the pipe pile behave similar to that of a circular foundation. Nevertheless, the pipe piles have a lower bearing capacity than that of the strip foundation for deep embedment ($d/t$>2-4). This may reflect the fact that the failure surface below the pile wall intersects the axis of symmetry about the toe depth, thus, not allowing shear stresses to be transferred to portions of the plug above the pile toe level.

In general, for the pipe piles ($D_o/t$ = 22 and 38) an apparently limit ultimate bearing capacity, $q_{uLim}$ is approached at some depth, hereafter referred to as critical embedment depth $d_{crit}$. This critical depth is, in fact, the transition depth from shallow embedment to deep embedment.

For embedment depth $d > d_{crit}$, the failure surface of the pile wall remains in a horizontal zone about the toe level and do not allow the failure surface to extend to the ground level. Therefore, the rock mass inside the pipe stops to contribute to the total rock mass resistance as it becomes kinematically able to pop up inside the pipe as a monolithic rock plug. At this moment, the pipe pile resembles a strip foundation that is embedded only on one side. As penetration continues, the pipe pile penetrates another $d_{crit}$ before the plug breaks and pops up again. Finally, one can expect that the plug is just a vertical stack of rock disks with a height of two to four times the pipe wall thickness, $d_{crit}$=2-4 $t$.

Another observation from the diagrams of the bearing capacity factor (Fig. 8) is that for embedment depths greater than $d_{crit}$, the pipe pile with $D_o/t$ = 38 has a higher bearing capacity than that of the pipe pile with $D_o/t$ = 22. This is because the latter allows for mobilization of shearing resistance over a larger zone of 19 times the wall thickness beneath the pipe wall in comparison with 11 times the pipe thickness for the pipe pile with $D_o/t$=22.

For circular pile ($D_o/t$ = 2) and nearly-strip foundations ($D_o/t$ = 8000), in weightless rock with practically null surcharge pressure, the solution by Serrano et al. [9] results in increasing bearing capacity values up to a limit embedment depth, thereafter, the failure envelope closes upon itself (Fig. 1) and the bearing capacity remains constant as seen in Fig. 8. Their analytical results are approximately valid up to 2 times pipe wall thickness, which is the range of interest for rock socketed piles and overestimates the bearing capacity with increasing embedment depth ($d/t$ > 2).

However, the numerical results (Fig. 8) for the circular and nearly strip foundations do not indicate approaching the limit embedment depth as suggested by [9]. The results indicate that the bearing capacity does not stop to increase with further embedment. The reason may be due to their postulated failure mechanism, which cannot be captured under the assumptions of this model: linear elasticity and perfectly nearly-associated plasticity. It is worth mentioning that the bearing capacity factors of the circular pile ($D_o/t$ = 2) for $d/t$ > 2 underestimate the theoretical ultimate values and are provided for sake of completeness.

The numerical results of the pipe piles in rock mass are in sharp contrast with the observations from model pipe pile tests in clay [40] which suggested that the correlations available for base capacity of closed-ended pipe piles can be transferred to the annular capacity of open-ended piles. A possible explanation to this contradiction can be the difficulty in separation of the pile skin friction and annular base resistance assuming that the pipe pile bearing response in rock and clay are similar.

## 6.2 Inclination of rock mass reaction at pipe tip

The unsymmetrical failure mechanisms shown in Fig. 7 for pipe piles ($D_o/t$ = 22 and 38) result in rock flow under the pipe wall. This in turn results in an inclined rock mass reaction at the pile tip tending to cause closure of the pipe as shown in Fig. 10. The reaction inclination has been assessed by integrating the normal and shear stress profiles immediately beneath the pipe wall. For shallow embedment ($d < d_{crit}$), the shear stresses approximately cancel each other around the pipe wall center indicating that almost equal amounts of rock flow on both sides. For deep embedment ($d > d_{crit}$), the rock tends to flow inwards over the whole pipe wall cross-section. As embedment depth increases, the load inclination angle increases and seems to approach a quasi-limit value as illustrated in Fig. 11. Inclination angle increases for lower pipe dimension ratios $D_o/t$. For $m_i$ > 5, the variation of the inclination angle with embedment depth does not seem to depend on $m_i$.

The radially inwards rock mass reaction on the pile tip increases with embedment depth and can reach a value as high as 22% of the ultimate vertical load depending on the rock mass strength. This force, if sufficiently large, can lead to pile closure and refusal in the case of driven piles. It is worth mentioning that a fully rough interface is assumed between the pipe toe and the rock mass. Consequently, the reaction inclination can be expected to reduce with a smoother interface.

### 6.3 Comparison with experimental data

Numerical results for bearing capacity enhancement with respect to embedment depth are compared with test data from impact driving and static penetration tests of model pipe tests. Holeyman [41] reported measured toe resistances of 60.3mm diameter instrumented model pipe piles that had been impact driven into synthetic rock specimens. Synthetic rock specimens were made of cement mortar and aerated autoclaved concrete (AAC), the mechanical properties of which are listed in Table 5. Neglecting the shaft friction, one can estimate the toe bearing resistance for the impact driven model pipe piles as shown in Fig. 13 together with the FEA results. The model pipe piles had dimension ratios of $Do/t$ = 22 and $Do/t$ = 38. Since all rock specimens were synthetic, they are assumed to be intact ($GSI$ =100).

For mortars, the Hoek-Brown parameter, $m_i$ can be estimated by fitting the Hoek-Brown failure envelope over the triaxial compression tests on mortar by Barbosa et al. [42] from which one would find $m_i$=5.5. From Fig.

13, it seems that the toe bearing resistances from the FE analysis bracket with a reasonable accuracy the test data of the model pipe piles driven into the different types of mortars. The FEA curves overestimate the experimental curves by almost 30% because the amount of settlement after each hammer blow might not have been enough to mobilize the peak resistance. As a result, the mobilized peak rock resistance depends on the hammer drop height. Due to the high porosity of the aerated autoclaved concrete (AAC), the H-B failure criterion does not seem appropriate to model its mechanical behavior. However, the results indicate that $m_i$ values between 1 and 2.5 may predict relatively well the toe bearing capacity of the model pipe pile driven into AAC (Fig. 13).

A series of static penetration tests of model pipe piles ($D_o$ = 60.3mm, $t$=1.6: $D_o/t$ = 38) were conducted into a block of calcarenite limestone from Saint-Maximin quarries located close to Paris in France. The rock is locally referred to as “Roche Douce”. For detailed microscope description of the rock mass, one can refer to Baud et al. [43]. The specimens were 15cm-prisms of octagonal base for which the diameter of the circumscribed circle was 45 cm. The height of the model pipe pile was 4cm. The model pipe pile, the limestone block and testing configuration can be seen in Fig. 14(a). The penetration rate was set to 90 μm/min. The speed was sufficiently low to mitigate rate effects. The tests were conducted under laboratory standard temperature of 20°. The uniaxial compressive strength of the rock mass is 6.8MPa (Standard Deviation, SD=1.7MPa) from cylindrical specimens with diameter of 60 mm and height of 150 mm. Besides, the splitting tensile strength is 1.0 MPa (SD=0.2MPa) from cylindrical disks with diameter of 60 mm and thickness of 23-34 mm [44]. The specimens were drilled from a similar limestone block as shown in Fig. 14(a).

The load-penetration diagrams are plotted in Fig. 15(a). The shaft resistance is estimated to be below 0.5 kN. The critical embedment depth, $d_{crit}$ presented in Section 6.1 can be clearly observed. The pipe pile bearing capacity increases with embedment up to the critical embedment (almost $3t$

here) thereafter, the rock plug pops up and the bearing capacity reduces to a value close to that of the pipe pile at surface. This sudden/gradual reduction in the bearing capacity could not be captured by the finite element analysis since linear elasticity with perfect plasticity is assumed. These cycles of rise and fall in the ultimate bearing capacity of the pipe pile continues as pipe penetrates deeper. This justifies to some extent the large band of scatter in the rock resistance curve for mortar, which was initially attributed to the possible heterogeneity of the mortar. The static penetration experiments confirm that the rock inside the tube consists of a vertical stack of individual rock layers with thickness of almost 2-4 times the pipe wall thickness as shown in Fig. 14(b) and (c). The number of troughs in the load-displacement diagram corresponds to the number of rock disks split from the cored rock.

Another important observation from the model pipe pile in limestone is that peak rock resistance increases initially with embedment depth and after a certain embedment depth, it actually diminishes. This contradicts what was observed in numerical simulations. The reason may be the assumption that the pipe pile is embedded/wished in place in the FE model hence eliminating the possible installation effects. The installation effects are beyond the scope of this paper. The rock mass at a certain depth may undergo some damage before the pipe tip reaches that depth. Despite the simplifying assumptions of the numerical model, the mechanism of plug formation is captured accurately. In addition, some insight is gained on the rock mass resistance.

To assess how the numerical results on bearing capacity enhancement can be applied to this particular experiment. One has to estimate the Hoek-Brown parameters of the rock mass. One can assume the limestone rock mass is intact ($GSI$=100) based on the joint and surface characteristics. The $m_i$ parameter can be determined from Eq. (8). This will lead to $m_i$=6.7. For a similar limestone, an $m_i$ = 7.1 has been reported from triaxial tests [15]. These values are consistent with those presented in Table 2 for sedimentary carbonate rocks. For GSI=100, the intact uniaxial compressive strength is equal to the measured uniaxial compressive strength, $\sigma_{ci}$=$\sigma_c$=6.8 MPa. The experimental load-displacement curves of Fig. 15(a) are normalized and superimposed on the FEA curves of bearing capacity factor (Fig. 8) for $D_o/t$=38 and plotted in Fig. 15(b). The numerical curves underestimate the rock mass resistance by almost 30%. This may be attributed to the scatter in uniaxial compressive strength data which had a coefficient of variation of 25%.

## 7 Conclusion

A numerical and experimental investigation of the annular base bearing capacity and failure patterns of typical pipe piles embedded in sedimentary rocks were conducted. The pipe piles were embedded in a homogeneous weightless isotropic rock mass obeying Hoek-Brown failure criterion. The pipe piles had dimension ratios, $D_o/t$ = 22 and 38 and their analysis results were compared against those of circular piles ($D_o/t$ = 2) and nearly-strip foundations ($D_o/t$ = 8000). The pile-soil interface is fully rough at the base and smooth on the shaft. The pile penetrates the rock mass in a fully unplugged mode. Design charts are provided for bearing capacity values of the pipe piles. They are employed in estimating rock mass resistance to penetration of model pipe piles. A summary of the results are hereby presented:

1. Toe bearing response of pipe piles should be investigated in two zones: shallow and deep embedment. The embedment depth at which the transition between these two zones occurs is a critical embedment depth $d_{crit}$. When the pipe reaches $d_{crit}$, the plug pops up and the pipe pile is like a strip foundation that is embedded only on one side. If penetration continues, the pipe pile penetrates another $d_{crit}$ before the rock mass breaks and pops up again inside the pipe. Finally, one can expect that the plug is just a vertical stack of rock disks with height equal to approximately two to four times the pipe wall thickness $d_{crit} = 2 - 4\ t$. This behavior was also confirmed through experimental data and

originates from the brittle nature of the rock mass.

2. At shallow embedment, the pipe pile is an intermediate case between strip and circular foundations approaching the strip foundation with increasing dimension ratio $D_o/t$. For deep embedment, the pipe pile response is more complex. For the desired range of pipe pile dimensions in piling operations i.e. $D_o/t$>18, the ultimate bearing capacity of a pipe pile approaches a limit value, which is less than or at most equal to that of an embedded strip foundation of width equal to the pipe wall thickness.
3. Failure mechanisms of the pipe piles is unsymmetrical. At shallow embedment, the failure mechanism extends to the surface. At deep embedment, the failure mechanism is local and consists of an acute triangular wedge under the pipe wall, a radial shear zone and a passive zone. An exit wedge forms inside the pipe. The unsymmetrical failure mechanism results in inclination of the rock mass reaction at the pile tip. The magnitude of this radially inward reaction at the pipe toe can reach up to 22% of the vertical limit load.
4. It is shown that an elastic perfectly plastic failure criterion with the adapted flow results in an acceptable approximation of the bearing capacity of the pipe pile since the problem is not very kinematically constrained but it fails to result in failure surfaces that close on the pile for circular piles and embedded strip foundation. The failure surfaces of this study extend to the ground surface overestimating the rock resistance in spite of the fact that the rock at the pile toe can fail in volumetric compression long before the shearing surface can reach to the ground level. An approach incorporating the inelastic compressibility of the rock at the pile tip is necessary for studying circular piles and embedded strip foundations.
5. Numerically, ultimate bearing capacity of the pipe piles increase by a factor of 1.3 to 1.5 with respect the surface and remains relatively constant thereafter. The depth factor depends mostly on the pipe

dimension ratio, $D_o/t$ and does not depend significantly on the Hoek-Brown parameter $m_i$.

6. Experimentally, ultimate bearing capacity of the pipe piles demonstrates a complex behavior, which is due to peculiar mechanism of plug formation. The peak rock mass resistance occurs after a penetration of around 3 times pipe wall thickness, thereafter, the rock mass resistance drops significantly and rises below the initial peak. Consequently, the practicing engineer may expect significant penetration once the pipe pile has been able to overcome the first peak resistance without damage. The peak rock mass resistance to pipe penetration can be estimated relatively well using the suggested design charts.

# 8 Acknowledgments

The support of the Walloon Region, Belgium represented by Mr. Pascal Lehance of the DG 04 of SPW is acknowledged. It allowed UCLouvain to develop an original laboratory setup and to perform model pile driving tests within the framework of the FONDEOLE Research Project (Subsidy Nr 1250394 for an industrial research of general interest). Calcarenite samples used for penetration testing have been graciously supplied by EDF Renouvelables, thanks to Mrs. Elisabeth Palix. Contributions from Prof. Benoît Pardoen, Henri de Chaunac, Antoine Watterman and members of LEMSC laboratory are also appreciated.

# 9 References

[1] Bowles JE. Foundation analysis and design. McGraw-hill; 1996.
[2] Hoek E. Strength of jointed rock masses. Géotechnique 1983;33:187–223.
[3] Hoek E, Carranza-Torres C, Corkum B. Hoek-Brown failure criterion-2002 edition. In: Proc. 5th North Am. Rock Mech. Symp. 17th Tunn. Assoc. Can. Conf. NARMS-TAC, Toronto; 7-10 July 2002. p. 267–273.
[4] Kulhawy FH, Carter JP. Settlement and bearing capacity of foundations on rock masses. Eng Rock Masses 1992:231–245.

[5] Merifield RS, Lyamin AV, Sloan SW. Limit analysis solutions for the bearing capacity of rock masses using the generalised Hoek–Brown criterion. Int J Rock Mech Min Sci 2006;43:920–937.
[6] Saada Z, Maghous S, Garnier D. Bearing capacity of shallow foundations on rocks obeying a modified Hoek–Brown failure criterion. Comput Geotech 2008;35:144–154.
[7] Clausen J. Bearing Capacity of Circular Footings on a Hoek–Brown Material: Loss of spatial consciousness? Int J Rock Mech Min Sci 2013;57:34–41.
[8] Serrano A, Olalla C. Ultimate bearing capacity at the tip of a pile in rock—part 1: theory. Int J Rock Mech Min Sci 2002;39:833–846.
[9] Serrano A, Olalla Marañón C, Galindo Aires RÁ. Ultimate bearing capacity at the tip of a pile in rock based on the modifed Hoek-Brown criterion. Int J Rock Mech Min Sci 2014;71:83–90.
[10] Meyerhof GG. The ultimate bearing capacity of foundations. Geotechnique 1951;2:301–332.
[11] De Beer EE. Experimental determination of the shape factors and the bearing capacity factors of sand. Geotechnique 1970;20:387–411.
[12] Liyanapathirana DS, Deeks AJ, Randolph MF. Numerical analysis of soil plug behaviour inside open-ended piles during driving. Int J Numer Anal Methods Geomech 1998;22:303–322.
[13] Hamdi S. Pipe pile driving into rock. PhD Thesis. UCLouvain, 2016.
[14] Hoek E. Practical rock engineering. 2007. Online Ed Rocscience 2007.
[15] Walton G, Arzua J, Alejano LR, Diederichs MS. A laboratory-testing-based study on the strength, deformability, and dilatancy of carbonate rocks at low confinement. Rock Mech Rock Eng 2015;48:941–958.
[16] Vardoulakis I, Sulem J. Application of bifurcation theory to rock mechanics problems. In: Comprehensive Rock Engineering JA Hudson, editor. Oxford: Pergamon Press; 1993. pp. 575–609.
[17] Carranza-Torres C, Fairhurst C. The elasto-plastic response of underground excavations in rock masses that satisfy the Hoek–Brown failure criterion. Int J Rock Mech Min Sci 1999;36:777–809.
[18] Yuan S-C, Harrison JP. An empirical dilatancy index for the dilatant deformation of rock. Int J Rock Mech Min Sci 2004;4:679–686.

[19] Zhao XG, Cai M. A mobilized dilation angle model for rocks. Int J Rock Mech Min Sci 2010;47:368–84.
[20] Alejano LR, Alonso E. Considerations of the dilatancy angle in rocks and rock masses. Int J Rock Mech Min Sci 2005;42:481–507.
[21] Rocscience Inc. Phase2 9.0 Manual 2018. https://www.rocscience.com/help/rs2/phase2_model/Strength_Parameters.htm (accessed October 25, 2018).
[22] Yin J-H, Wang Y-J, Selvadurai APS. Influence of nonassociativity on the bearing capacity of a strip footing. J Geotech Geoenvironmental Eng 2001;127:985–989.
[23] Houlsby GT. How the dilatancy of soils affects their behaviour. University of Oxford; 1991.
[24] Vermeer PA, van Langen H. Soil collapse computations with finite elements. Ing-Arch 1989;59:221–36.
[25] Van Baars S. 100 YEARS OF PRANDTL'S WEDGE. IOS Press; 2018.
[26] De Borst R, Vermeer PA. Possibilites and limitations of finite elements for limit analysis. Géotechnique 1984;34:199–210.
[27] Yahia-Cherif H, Mabrouki A, Benmeddour D, Mellas M. Bearing capacity of embedded strip footings on cohesionless soil under vertical and horizontal loads. Geotech Geol Eng 2017;35:547–558.
[28] Loukidis D, Chakraborty T, Salgado R. Bearing capacity of strip footings on purely frictional soil under eccentric and inclined loads. Can Geotech J 2008;45:768–87.
[29] Manoharan N, Dasgupta SP. Bearing capacity of surface footings by finite elements. Comput Struct 1995;54:563–586.
[30] Hoek E, Diederichs MS. Empirical estimation of rock mass modulus. Int J Rock Mech Min Sci 2006;43:203–15.
[31] Gercek H. Poisson's ratio values for rocks. Int J Rock Mech Min Sci 2007;44:1–13.
[32] Brinkgreve RBJ, Kumarswamy S, Swolfs WM, Zampich L, Ragi Manoj N. Plaxis 2019 - Finite element code for soil and rock analysis. Netherlands: PLAXIS bv; 2019.
[33] Koiter WT. Stress-strain relations, uniqueness and variational theorems for elastic-plastic materials with a singular yield surface. Q Appl Math 1953;11:350–354.
[34] Clausen J, Damkilde L, Andersen LV. Robust and efficient handling of yield surface discontinuities in elasto-plastic finite element calculations. Eng Comput 2015;32:1722–1752.

[35] Abbo AJ, Lyamin AV, Sloan SW, Hambleton JP. A C2 continuous approximation to the Mohr–Coulomb yield surface. Int J Solids Struct 2011;48:3001–3010.

[36] Huang J, Griffiths DV. Observations on return mapping algorithms for piecewise linear yield criteria. Int J Geomech 2008;8:253–265.

[37] Langen HV, Vermeer PA. Automatic step size correction for non-associated plasticity problems. Int J Numer Methods Eng 1990;29:579–98.

[38] Cook RD. Concepts and applications of finite element analysis. John wiley & sons; 2007.

[39] Rudnicki JW, Rice JR. Conditions for the localization of deformation in pressure-sensitive dilatant materials. J Mech Phys Solids 1975;23:371–394.

[40] Lehane BM, Gavin KG. Base Resistance of Jacked Pipe Piles in Sand. J Geotech Geoenvironmental Eng 2001;127:473–80.

[41] Holeyman A. Battage de pieux métalliques dans la roche. Rev Fr Géotechnique 2017:1.

[42] Barbosa CS, Lourenço PB, Mohamad G, Hanai JB. Triaxial compression tests on bedding mortar samples looking at confinement effect analysis. In: Proc. 10th North American Masonry Conf., St. Luis, Missouri; 3-5 June 2007. p. 992-1002.

[43] Baud P, Vinciguerra S, David C, Cavallo A, Walker E, Reuschlé T. Compaction and failure in high porosity carbonates: Mechanical data and microstructural observations. Pure Appl Geophys 2009;166:869–898.

[44] Bosco J, Vander Elst M. Calcarenite used as foundation material for windmills. Thesis. UCLouvain, 2018.


## 10 List of Figures

# 11 List of Tables

Table 4 – Comparison of surface bearing capacity values from FE analysis with some published results

Table 5 – Properties of the synthetic rock specimens after [41]

## 12 Figures

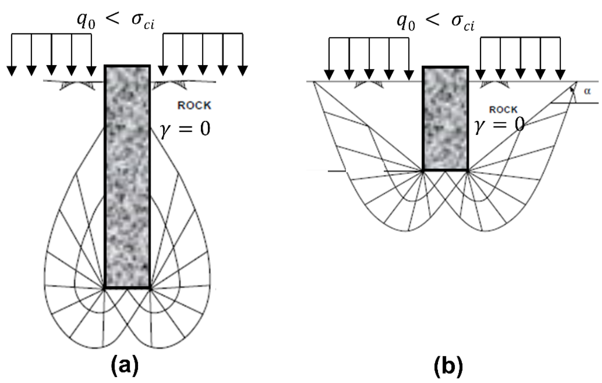


*Fig. 1* – Postulated failure mechanisms for (a) deep and (b) shallow piles with surcharge pressure at the embedment depth less than uniaxial compressive strength of the intact rock after *[8]*

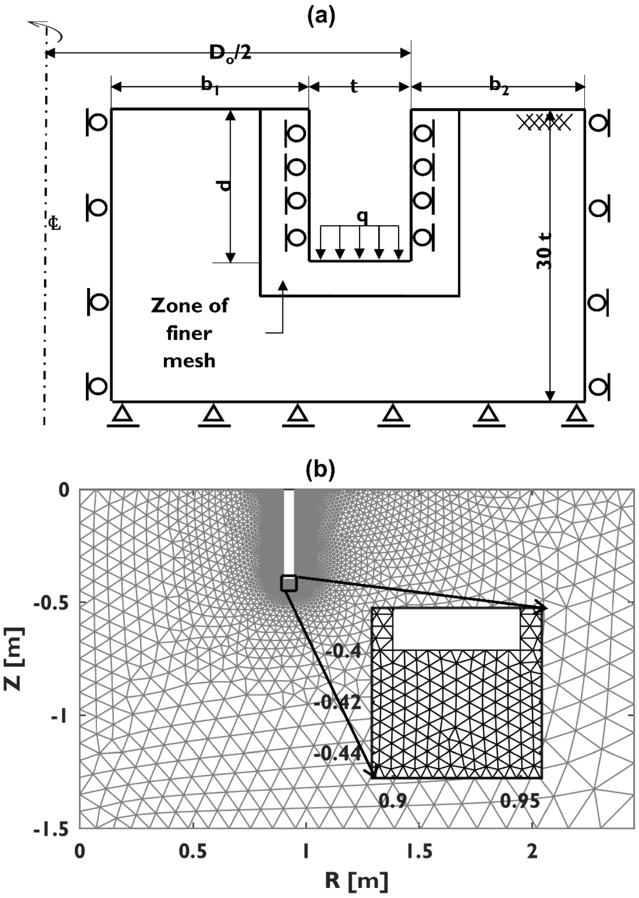


*Fig. 2* – (a) Idealized axisymmetric geometry and boundary conditions of the problem and (b) a typical model mesh for $D_o$/t=38 and d/t=8

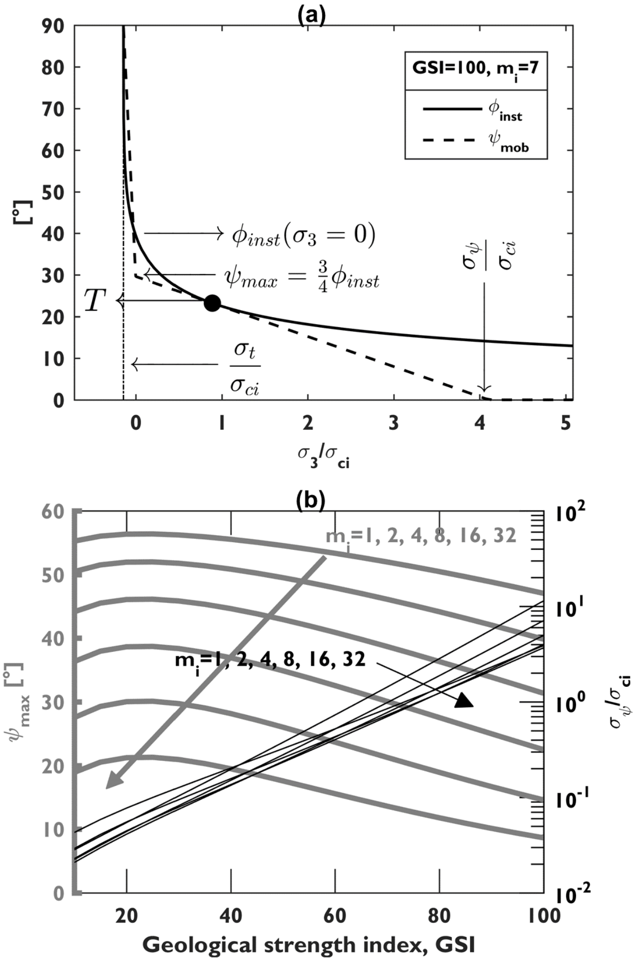


*Fig. 3* – (a) Friction angle and mobilized dilatancy angle against normalized confining stresses for a typical Hoek-Brown failure envelope and (b) parameters of the adopted flow rule against GSI and $m_i$

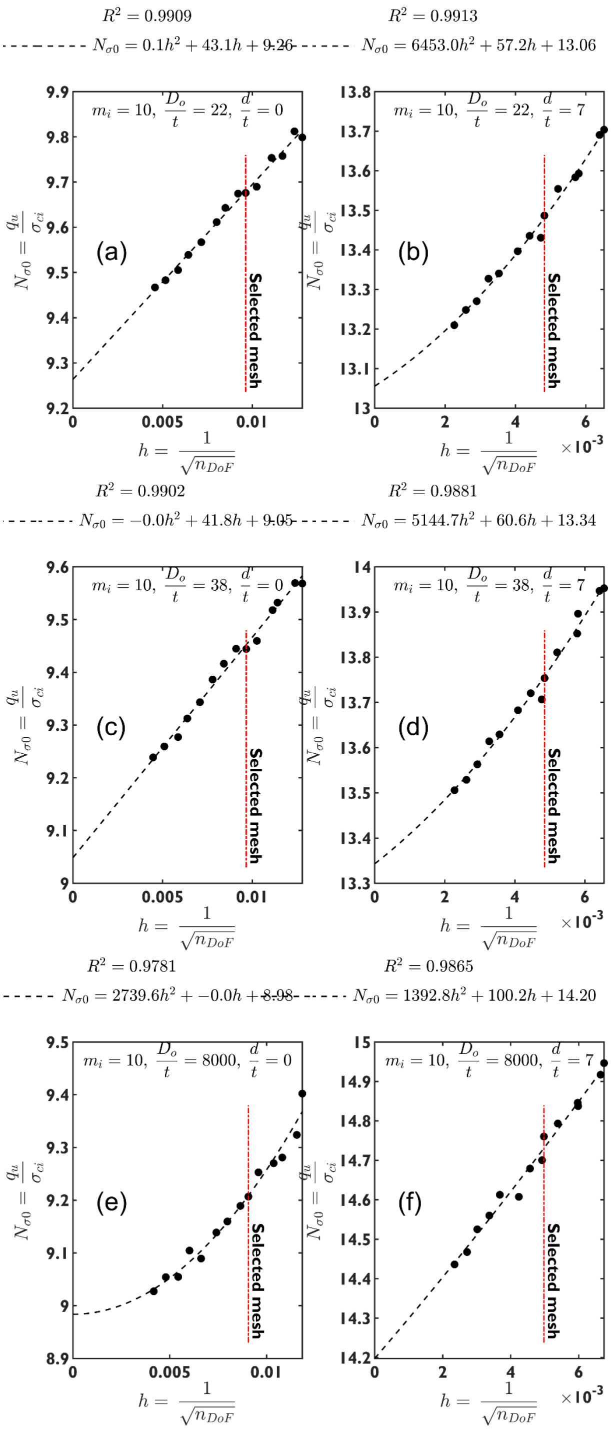


*Fig. 4* – Effect of the number of model degrees of freedom on the computed bearing capacity factor for various pipe pile geometries embedded in the reference Hoek-Brown material

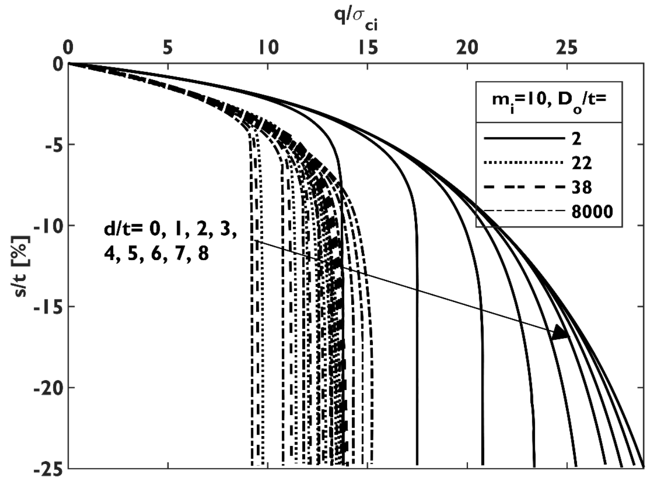


*Fig. 5* – Typical diagrams of normalized average vertical pressure at pile tip against relative settlement

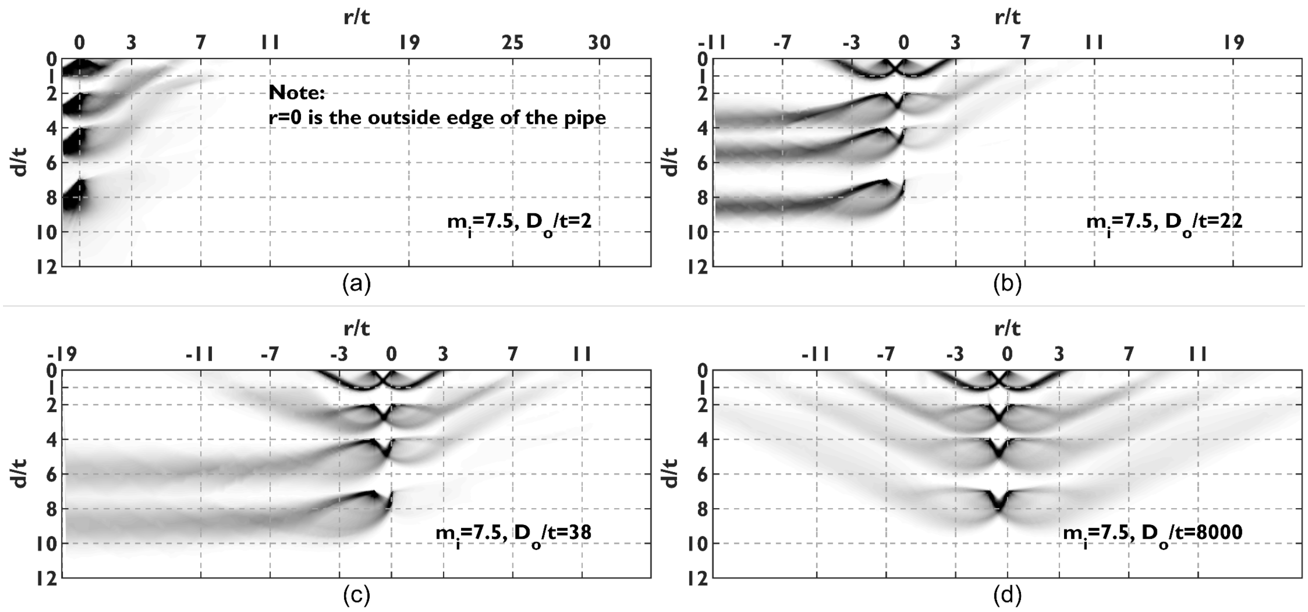


*Fig. 6* – Effect of embedment and pipe geometry on the failure mechanism under piles embedded in the reference H-B material with a typical $m_i$ (a) circular pile (b)(c) pipe piles and (d) nearly strip foundation (shading not to scale)

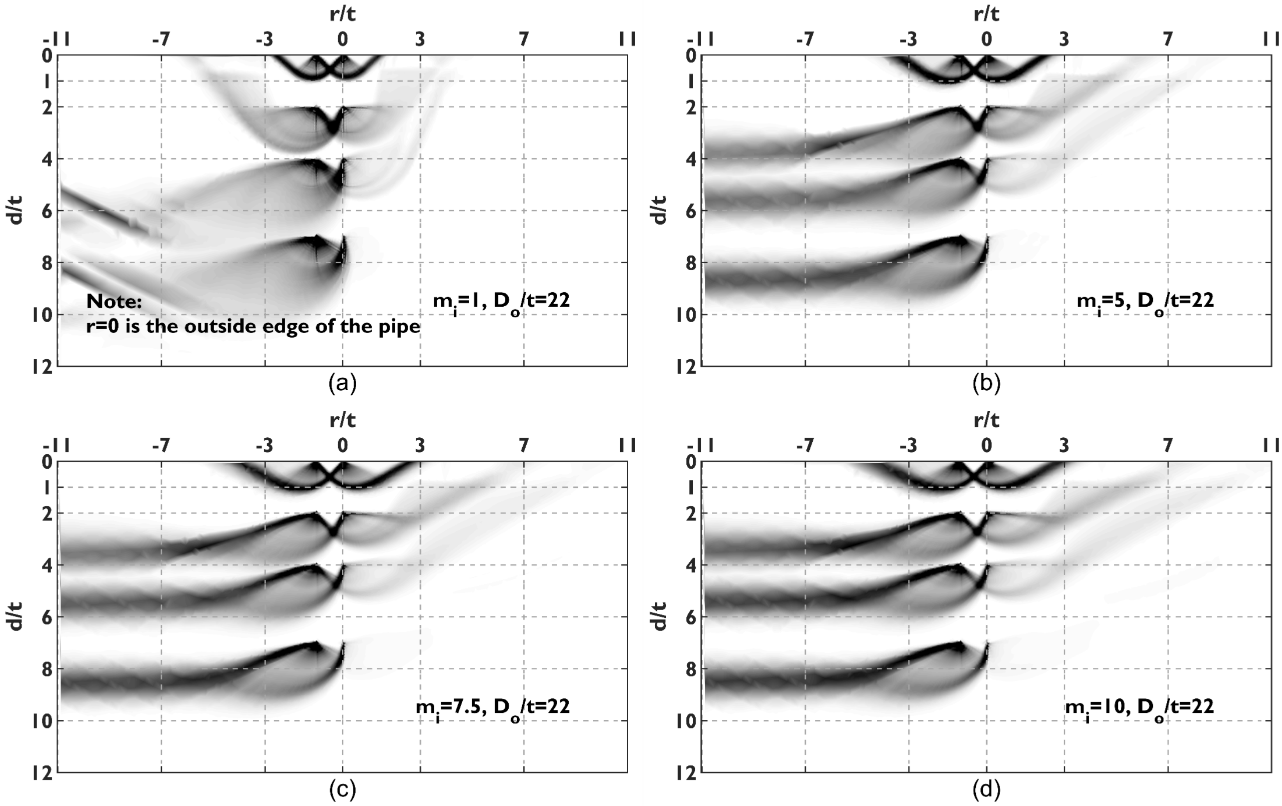


*Fig. 7* – Effect of embedment and $m_i$ parameter on the failure mechanism under a typical pipe pile in the reference H-B material (shading not to scale)

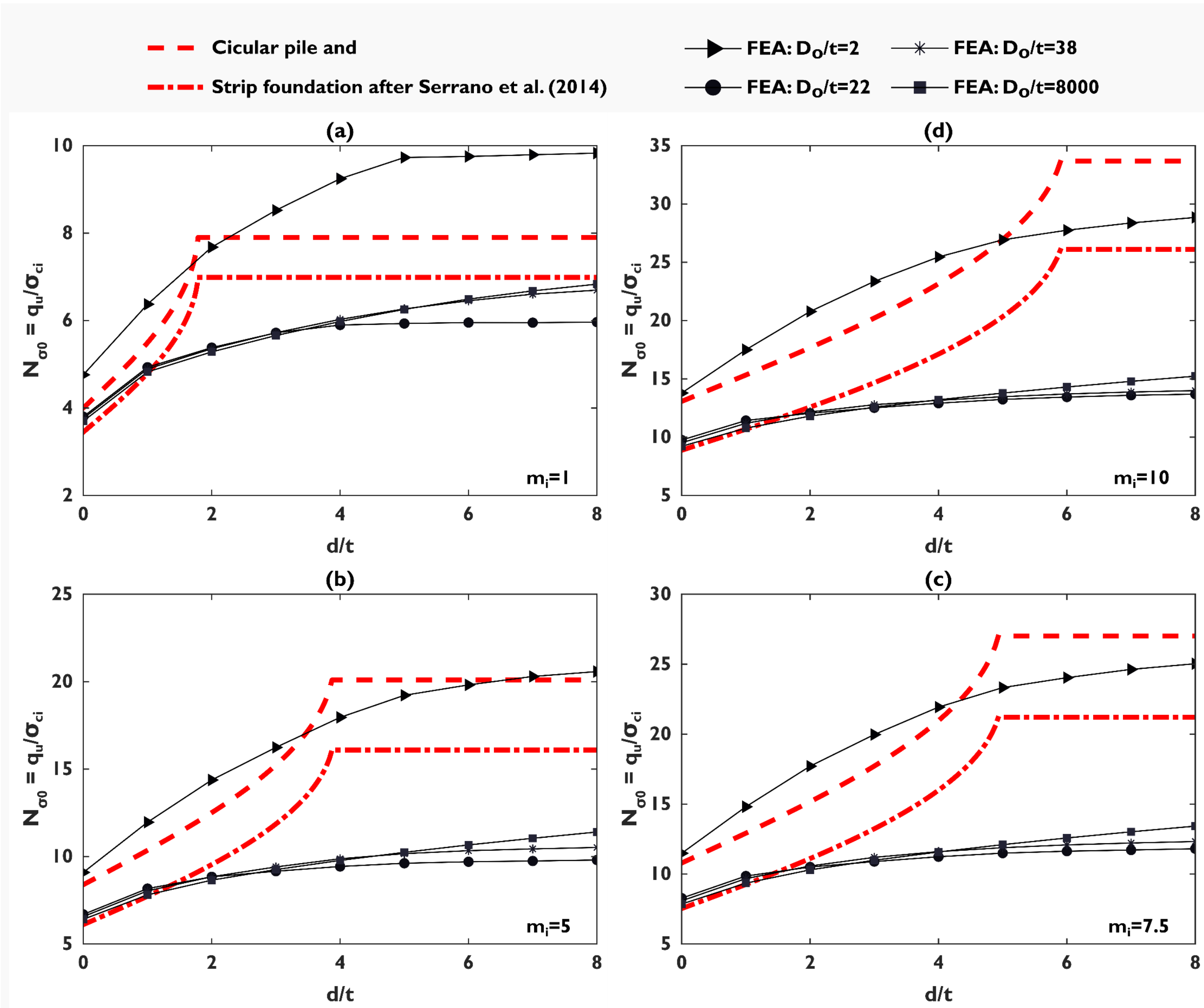


*Fig. 8* – Influence of pipe geometry and parameter $m_i$ of the reference Hoek-Brown material on global bearing capacity factor against normalized embedment depth

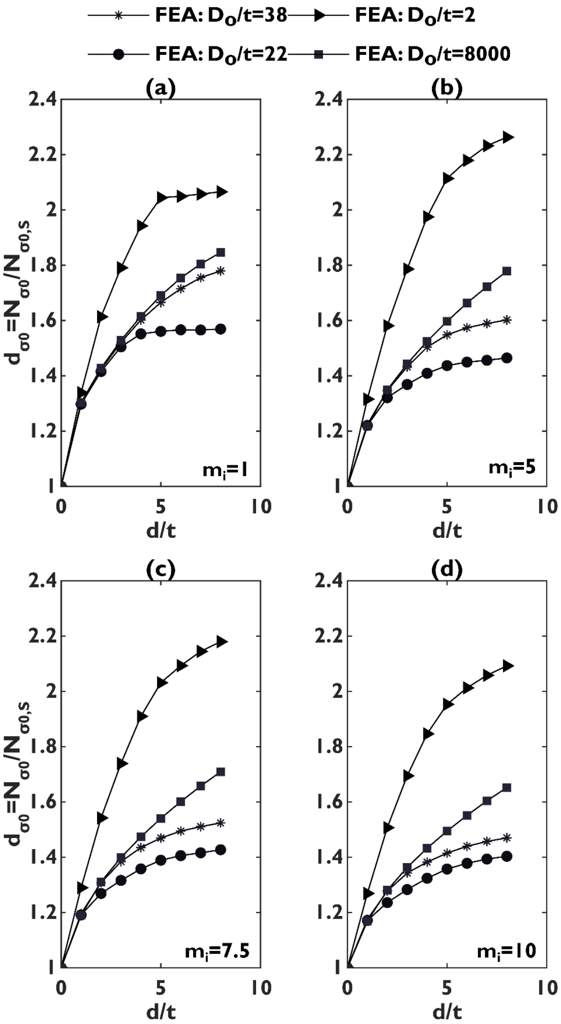


Fig. 9 – Effect of pipe geometry and mi parameter of the reference Hoek-Brown material on the depth factor against normalized embedment depth

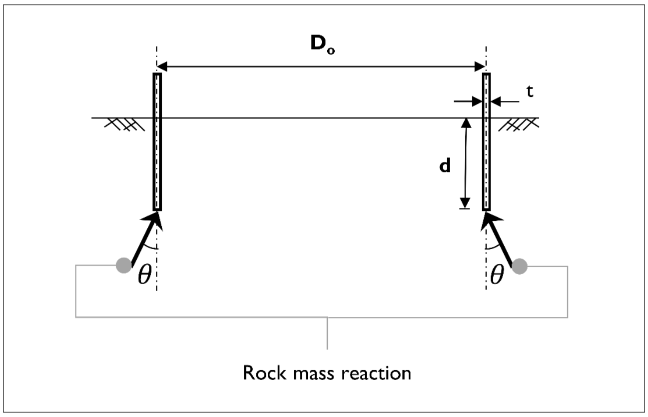


*Fig. 10* – Idealized inclined rock mass reaction at the pile tip due to unsymmetrical failure mechanism around pile wall center

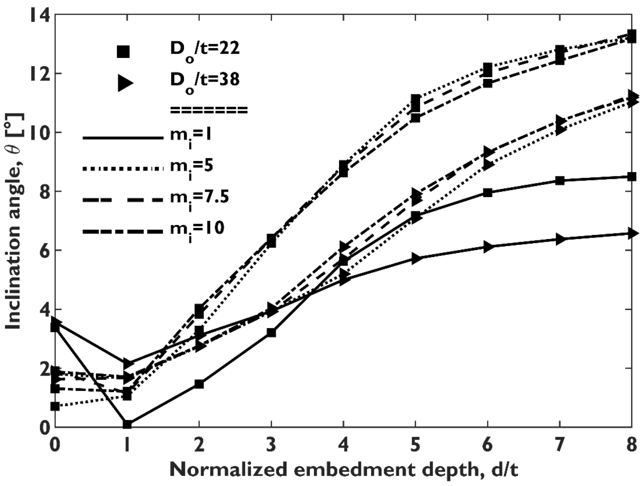


*Fig. 11* – Role of pipe geometry, embedment and $m_i$ parameter of the reference Hoek-Brown material on the inclination of the rock mass reaction at the pipe tip

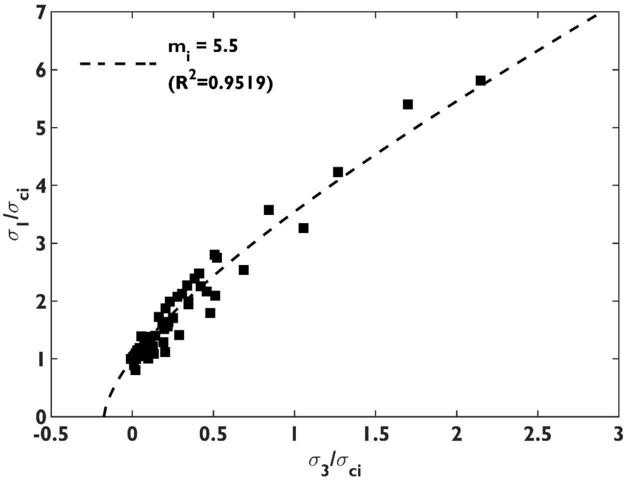


*Fig. 12* – Best fit of the Hoek-Brown failure criterion on mortar triaxial test data after *[42]*

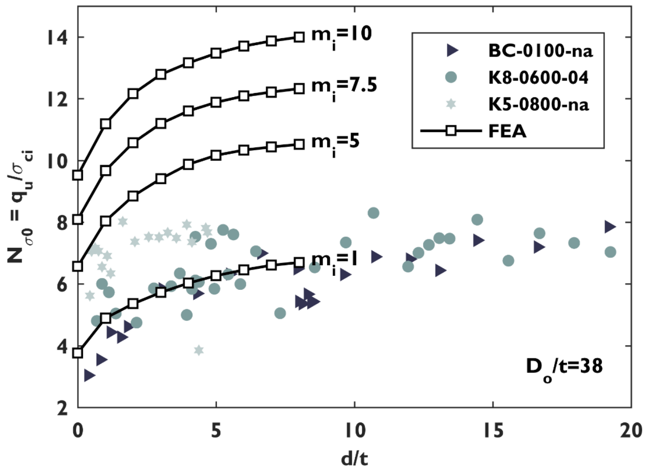


*Fig. 13* – Normalized measured and computed depth profiles of bearing capacity for a model pipe pile impact-driven into synthetic rocks (data after *[41]*)

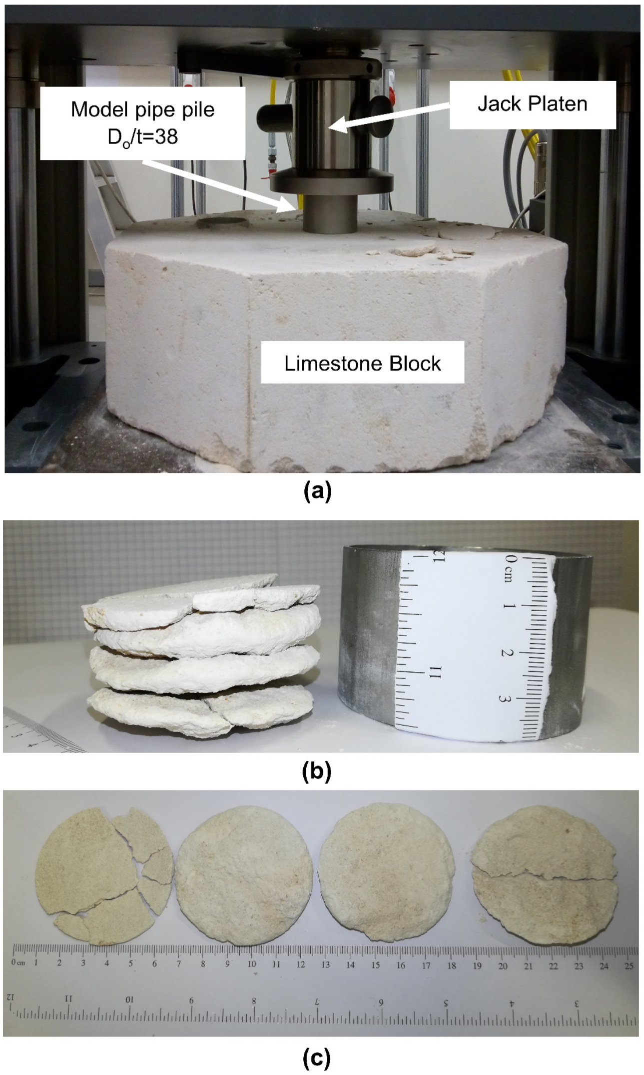


*Fig. 14* – (a) Load test arrangement (b) side view and (c) top view of the retrieved rock plug for Specimen #6 consisting of vertical stack of rock disks (Fines are removed for clarity)

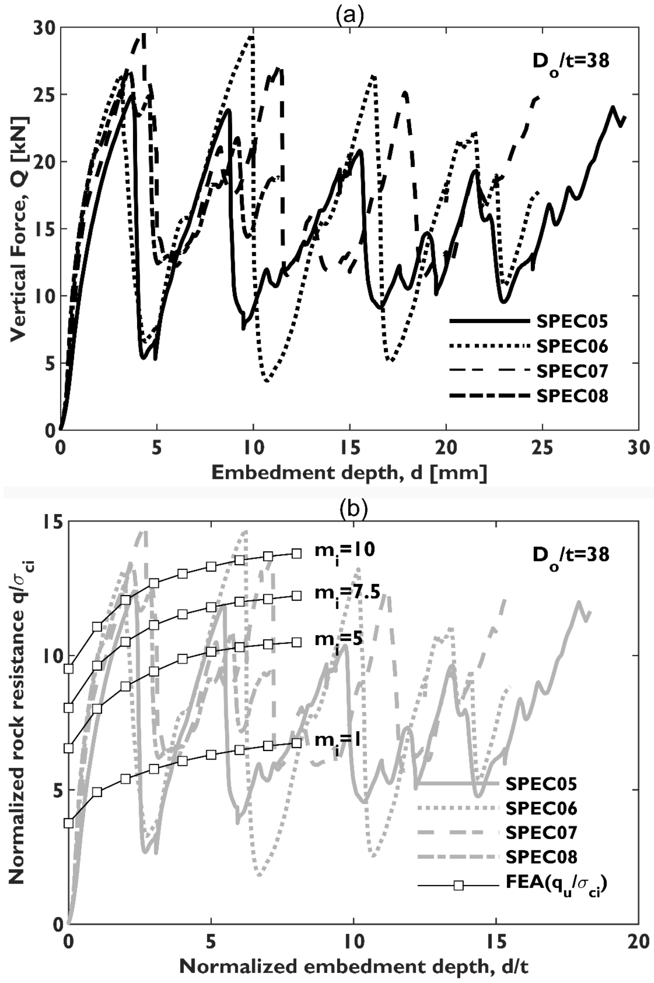


*Fig. 15* – (a) Depth profile of rock mass resistance as model pipe pile penetrates limestone block and (b) Comparison of normalized experimental data with the FEA results

# 13 Tables

Table 1 – Details of model geometry

| | $D_o/t = 2$ (circular) | $D_o/t = 22$ (pipe) | $D_o/t = 38$ (pipe) | $D_o/t = 8000$ (nearly strip) |
|---|---|---|---|---|
| $b_1/t$ | 0 | 11 | 19 | 30 |
| $b_2/t$ | 30 | 30 | 30 | 30 |

Table 2 - Typical values of the material constant, $m_i$ for rock masses obeying the H-B failure criterion after *[14]*

| Rock type | Class | Group | Texture | | | |
|---|---|---|---|---|---|---|
| | | | Coarse | Medium | Fine | Very fine |
| Sedimentary | Clastic | | Conglomerate (21 ± 3) | Sandstone (17 ± 4) | Siltstone (7 ± 2) | Claystone (4 ± 2) |
| | | | Breccia (19±5) | | Greywacke (18 ± 3) | Shale (6 ± 2) |
| | | | | | | Marl (7 ± 2) |
| | Non -clastic | Carbonate | Crystalline Limestone (12 ± 3) | Sparitic Limestone (10 ± 2) | Micritic Limestone (9 ± 2) | Dolomite (9 ± 3) |
| | | Evaporite | | Gypsum (8 ± 2) | Anhydrite (12 ± 2) | |
| | | Organic | | | | Chalk (7 ± 2) |

Table 3 – Flow rule parameters for the reference Hoek-Brown material

| $m_i$ | $\psi_{max}$ [°] | $\sigma_\psi/\sigma_{ci}$ |
|---|---|---|
| 1 | 8.7 | 11.40 |
| 5 | 25.3 | 4.55 |
| 7.5 | 30.5 | 4.04 |
| 10 | 34.2 | 3.82 |

Table 4 – Comparison of surface bearing capacity values from FE analysis with some published results

(a) Strip foundation

| $m_i$ | $N_{\sigma 0}$ ($q_u = N_{\sigma 0}\,\sigma_{ci}$) after [5] | $N_{\sigma 0}$ ($q_u = N_{\sigma 0}\,\sigma_{ci}$) after FEA $D_o/t = 8000$ | Relative difference % |
|---|---|---|---|
| 5 | 6.12 | 6.41 | 4.7 |
| 10 | 8.90 | 9.22 | 3.6 |

(b) Circular foundation

| $m_i$ | $N_{\sigma 0}$ ($q_u = N_{\sigma 0}\,\sigma_{ci}$) after [7]* | $N_{\sigma 0}$ ($q_u = N_{\sigma 0}\,\sigma_{ci}$) after FEA $D_o/t = 2$ | Relative difference % |
|---|---|---|---|
| 5 | 9.03 | 9.09 | 0.7 |
| 7.5 | 11.25 | 11.49 | 2.1 |
| 10 | 13.43 | 13.79 | 2.7 |

*Value interpolated from charts

Table 5 – Properties of the synthetic rock specimens after *[41]*

| Specimen Designation | Material Type | Age [day] | Porosity (%) | $\sigma_{ci}$ [MPa] | $\sigma_{ti}$ [MPa] |
|---|---|---|---|---|---|
| BC-0100-na | AAC | >90 | >60 | 4.2 | 0.6 |
| BC-0910-na | AAC | >90 | >60 | 4.2 | 0.6 |
| K5-0800-na | Mortar | - | 3-5 | 16 | - |
| K8-0600-04 | Mortar | 4 | 3-5 | 11 | - |